Chapter 6

Fe_3O_4 and ZnCoO Based Magnetic Tunnel Junctions

6.1 Introduction

In this chapter, we focus on the fabrication of full oxide magnetic tunnel junctions (MTJs). The MTJ stacks were in the form of Fe_3O_4/MgO/ZnCoO, which were fabricated by ion beam deposition. This chapter described the combination of the two materials we studied in the pervious chapter. In the first part, we described the consideration and improvement of the layer structure. In the second part, the magnetic properties and MR behavior of these full stack MTJs will be introduce.

In the previous chapter, we already demonstrated the room temperature fabrication of epitaxial Fe_3O_4 (111) and ZnCoO (0002) with introducing the Cu underlayer by ion beam deposition. Because of the relative high resistance of the Fe_3O_4 and ZnCoO as the electrodes, a good conductivity of Cu underlayer could help us to solve the problem of non-uniform current distribution in the MTJ device.

However, in a conventional MTJ, high temperature post-annealing (~250℃) is a necessary process to define the pinned layer direction. Besides, the post annealing process could also improve the quality and MR ratio of the MTJs. Especially in MgO-based MTJs, high temperature annealing process (even higher then 400 ^{o}C) could effectively

improve the crystalline quality of the MgO tunneling barrier. However, if the annealing temperature is higher than 150 ^{o}C, large amount of the $CuSi_x$ will form at the interface between the Cu underlayer and Si substrates. These $CuSi_x$ would greatly increase the roughness of the electrode. On the other hand, the Cu layer is difficult to remove during the etching process. Therefore, in this chapter, we will try to further improve the layer structure.

In recent years, an extremely high MR was observed from MTJs fabricated by using crystalline MgO as a tunnel barrier. [1,2] The origin of such a high MR is the symmetry of a electron wave functions and accompanied coherent spin-polarized tunneling. MTJs with highly oriented MgO (001) tunnel barrier and CoFe electrode were fabricated by Parkin *et al*. [1] These MTJs exhibit MR as high as ~220% at room temperature and ~300% at low temperature. The values of the MR of MgO-based MTJs are about three times higher than the MR in any other type of MTJs. This achievement clearly represented a breakthrough.

We should remark that MgO has an excellent crystal lattice matching with Fe_3O_4. Highly quality epitaxial Fe_3O_4 films could be grown on MgO substrates. Therefore, one might expect high tunneling MR in Fe_3O_4/MgO/Fe_3O_4 or Fe_3O_4/MgO/Fe MTJs. Therefore, we chose the MgO as the tunneling barrier. Half metal –Fe_3O_4 and DMS – ZnCoO were integrated into MgO-based MTJs.

6.2 Experimental Procedures

Full stack of the MTJs were grown on Si (001) substrates with 200 nm SiO_2 at room temperature by using a RF ion beam deposition system. The base pressure of IBD was 2×10^{-7} Torr and the working pressure were maintained at 3×10^{-4} Torr. A composite target composed of a ZnO target and Co chips was used for ZnCoO deposition. All the other oxide films were prepared from the oxide target. Pure Ar gas was introduced into the chamber when the thin films were prepared.

Film structures were characterized by an X-ray diffractometer (XRD). The Co concentration of ZnCoO films was determined by inductively coupled plasma-mass spectrometry (ICP-MS). Magnetic and magneto-transport properties were investigated by using a superconducting quantum interference device (SQUID) and a physical property measurement system (PPMS), respectively.

6.3 Results

6.3.a Fabrication of ZnCoO and Fe_3O_4

In order to improve the quality of oxide thin film, we replace the DC source with RF source in the ion beam deposition system. For the oxide-type targets, the RF source could provide more stable beam current and beam voltage during the oxide thin film depositions. Fig. 6.1 showed the XRD scans of SiO_2//ZnO 50 nm, a clear (0002) ZnO peak could be observed. It means the well texture of ZnO could be directly deposited on the SiO_2 substrate; it may be due to the relative small working pressure and the higher mobility of the sputtered atoms. The well texture of ZnO films prepared from the RF-IBD system was just proving the RF source was more suitable for oxide system. In order to fabricate the ZnCoO films, we used the composite target composed of Co chips and ZnO target. The Co concentration of ZnCoO was 7% determined by the ICP-MS. We will discuss the magnetic properties of ZnCoO and valence state of Co in ZnCoO in the next section.

Since ZnO revealed the well texture on SiO_2 substrate, we prepared the Fe_3O_4 films on this buffer layer. Fig. 6.2 showed the XRD scans of SiO_2//ZnO 50 nm/ Fe_3O_4 50 nm, a clear (111) Fe_3O_4 peak could be observed. The valence state of Fe in Fe_3O_4 layer would be discussed in the next section.

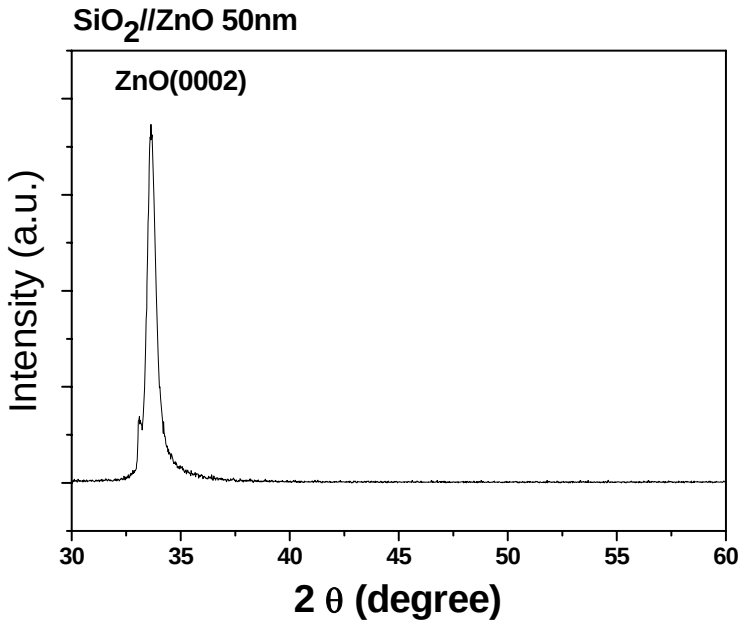

Fig. 6.1. XRD scans of SiO_2//ZnO 50 nm

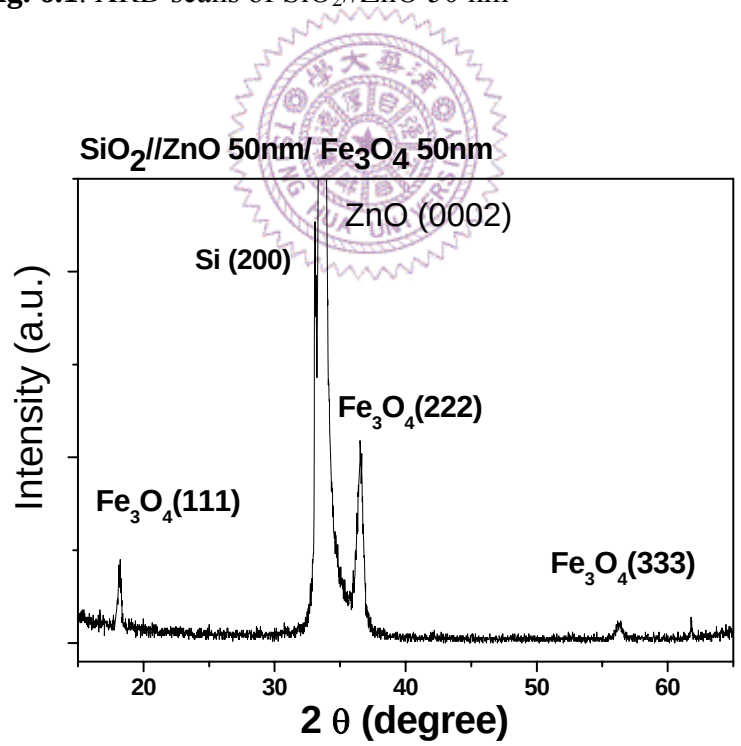

Fig. 6.2. XRD scans of SiO_2//ZnO 50 nm/Fe_3O_4 50nm

6.3.b Identification of Fe_3O_4 and ZnCoO

Fe_3O_4

Although the structure of the Fe_3O_4 was characterized, it is worthy to notice that the γ-Fe_2O_3 (maghemite) has the same cubic structure (inverse spinel) and similar lattice constants (a= 0.835 nm) to the Fe_3O_4 (a= 0.839 nm). It is quite challenging to only use XRD patterns to conclusively exclude the existence of γ- Fe_2O_3 in the film. To verify the phases, x-ray magnetic circular dichroism (XMCD) was performed to analyze the chemical states and magnetic moment alignment of Fe.

XMCD data were recorded by using the high-energy beamline 11A1 at the National Synchrotron Radiation Research Center in Taiwan. The XMCD spectra were obtained in a total electron yield mode with an 80Å probing depth. The samples were introduced in an UHV experimental chamber. The pressure during the measurements was below 1 *10^{-9} Torr, and the sample temperature was varied from 300 K to 10 K.

Before discussing the XMCD experiment data, the configuration of Fe valence state in Fe_3O_4 was needed to briefly describe. Fe_3O_4 could be represented as $Fe^{3+}(Fe^{2+}Fe^{3+})O_4$, where the parentheses indicated cations in octahedral (O_h) sites as opposed to tetrahedral (T_d) sites. A schematic of the Fe_3O_4 lattice is shown in the Fig. 6.3. In the other word, the Fe^{3+} ions are in the tetrahedral sites and a mixture of Fe^{2+} and Fe^{3+} in octahedral lattice sites.

Fig. 6.4 revealed the Fe 2*p* XAS (x-ray absorption spectrum) result for Fe_3O_4 layer with parallel and antiparallel alignments of the light

helicity vector to the projected component of sample magnetization [3]. Reversal of the magnetizations has the same effect as reversal of the light helicity vector. The XMCD signal is characterized by three contributions as shown in the Fig. 6.5. The contribution from Fe^{2+} and Fe^{3+} spin-up ions on octahedral sites are seen as negative peaks at the Fe L_3 absorption edge and positive peaks in the Fe L_2 edge. The octahedral Fe ions could be distinguished by their oxidations state in XMCD. The Fe^{3+} spin-down ions on tetrahedral sites are seen as a positive peak at the Fe L_3 edge and a negative peak at the Fe L_2 edge [4].

These relative intensities are given with respect to pure Fe_3O_4. Our experiment results agree with the pervious data reported by Morral et al. [4] as shown in the Fig. 6.6. In their works, Fe_3O_4 (111) thin films were prepared on an ordered Pt (111) surface. The Fe_3O_4 film was grown by first depositing pure Fe at room temperature, and then it was oxidized for 5 min at an O_2 atmosphere at 830K. Finally, stoichiometry of Fe_3O_4 was confirmed by using the conventional electron Mössbauer spectroscopy (CEMS). The relative peaks intensities and line shape in XMCD spectrum, which could help us to determine the ratio for Fe_{Oh}^{2+} : Fe_{Td}^{3+} : Fe_{Oh}^{3+} was 1:1:1.

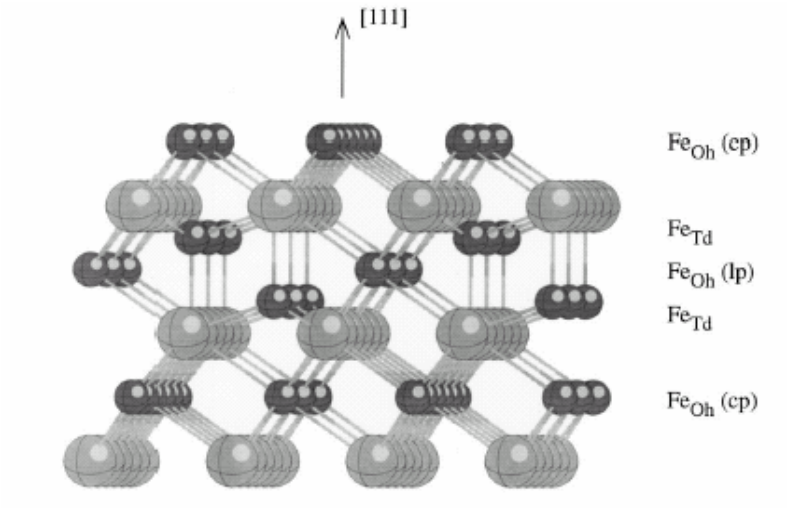

Fig. 6.3. A schematic of the Fe_3O_4 lattice [3]

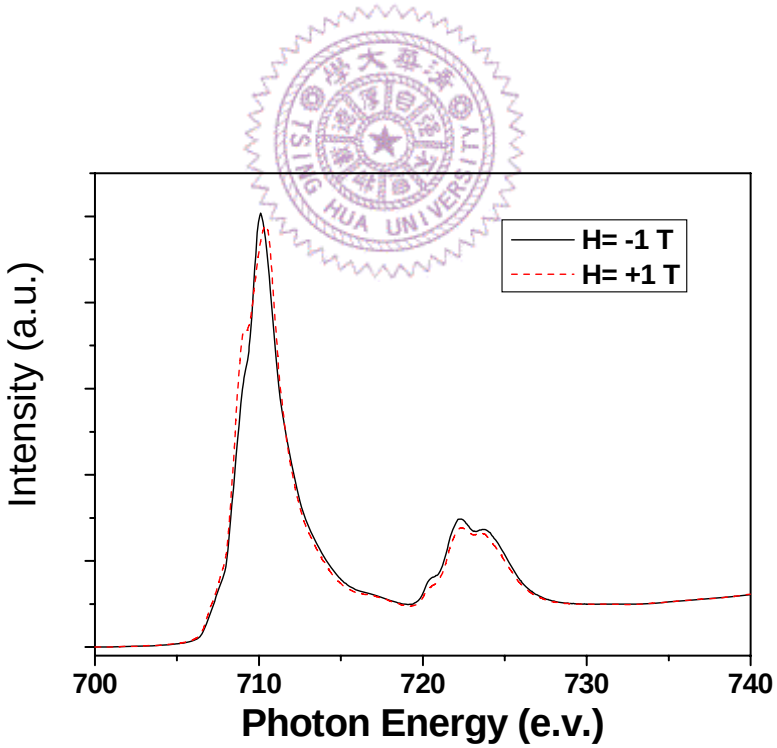

Fig. 6.4. The Fe 2*p* XAS (x-ray absorption spectrum) result for Fe_3O_4 layer with parallel and antiparallel alignments of the light helicity. vector to the projected component of sample magnetization.

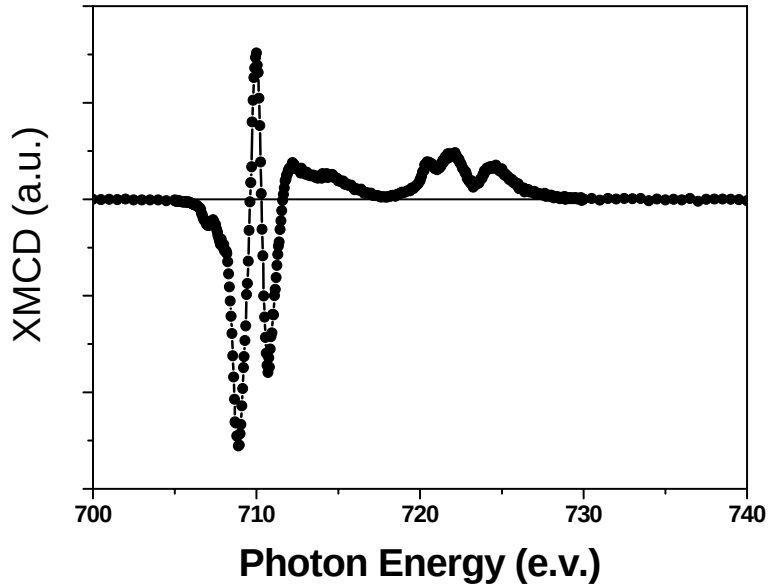

Fig. 6.5. The XMCD signal of Fe_3O_4 50nm

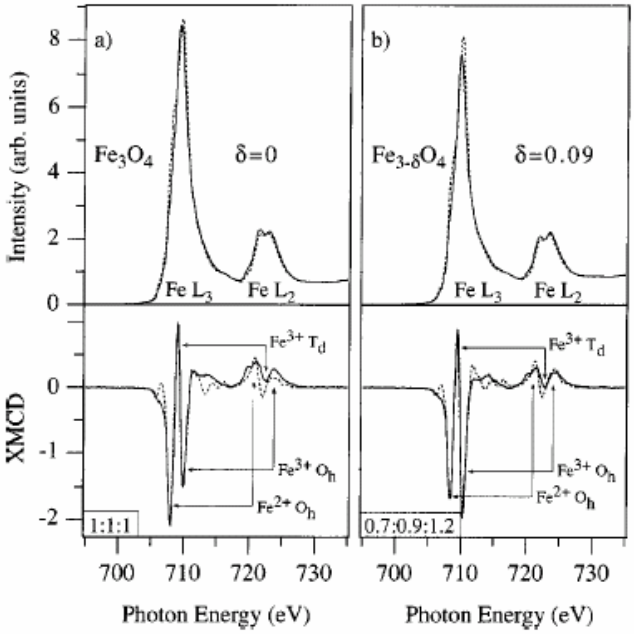

Fig. 6.6. The XMCD signal of pure and over oxidation of Fe_3O_4 [3]

ZnCoO

In this part, XAS (x-ray absorption spectrum) was performed to identify the valence state of Co in the ZnCoO. As shown in the Fig 6.7, the spectrum of $ZnCo_{0.07}O$ reveals only L_2 edge of the Co^{2+} state locating at 781 eV and no metallic Co peak at 778 eV. In addition, no metallic Co clusters can be observed in TEM images. The line shape of the spectrum was also similar to the spectrum of Co^{2+} state. In addition, the room-temperature hysteresis loop, shown in Fig. 6.8, clearly demonstrated the ferromagnetic characteristic of highly texture ZnCoO films.

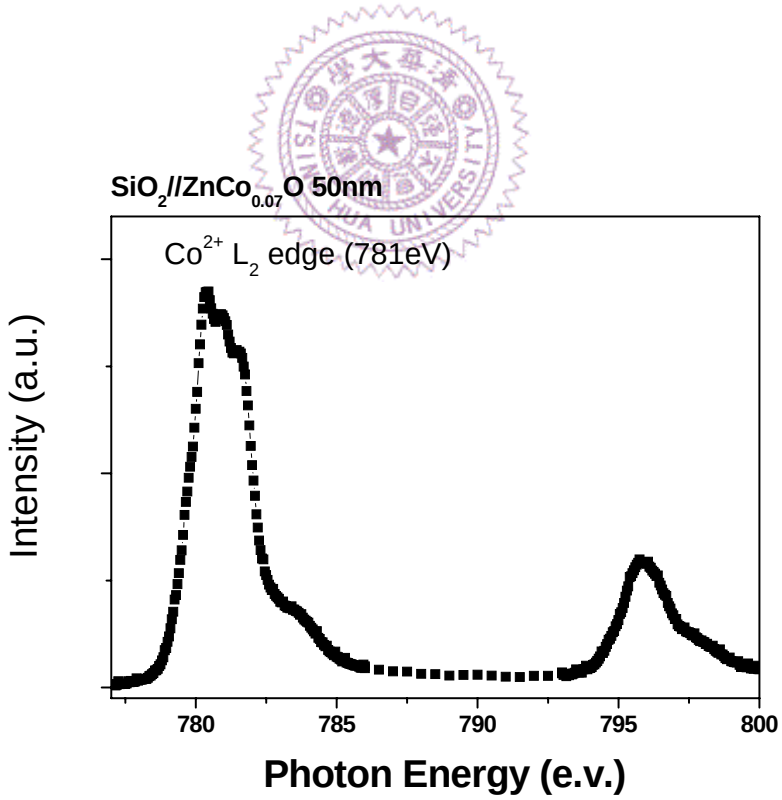

Fig. 6.7. The Co L_2 XAS data for ZnCoO layer

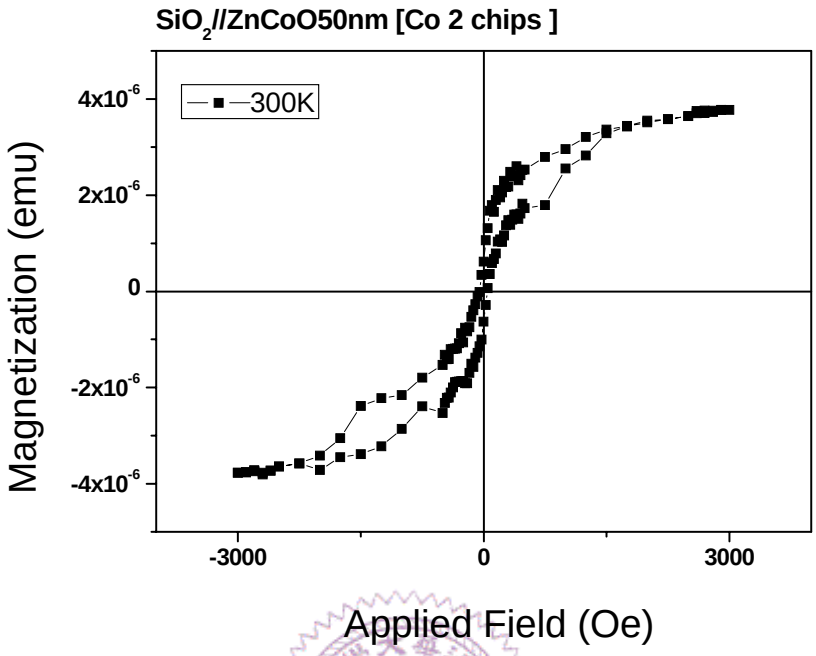

Fig. 6.8. Hysteresis loop of $ZnCo_{0.07}O$ films measured at 300 K

6.3.c Improvement of underlayer

In this section, we would discuss the improvement of underlayer of the MTJ. The basic requirement of the underlayer should include the conducting electrode and structural buffer layer. In the first step, the NiO, MgO and TiN were deposited on the ZnO structural buffer layer, respectively. As shown in Fig. 6.9, the XRD patterns of SiO_2//ZnO 50nm/ MgO 50nm, indicated a good out-of-plane (002) texture of MgO films on (0002) ZnO underlayers, respectively. As we mentioned before, the MR (MagnetoResistance) ratio of MgO-based MTJs strongly depended on the crystalline quality of the MgO barrier. In most studies, in order to obtain the epitaxial MgO barrier, the full stacks of MTJs were deposited on the (002) MgO substrate. However, the MgO substrate was too expensive to be used in a conventional device. Therefore, the well texture (002) of MgO underlayer could be obtained on SiO_2 substrates by introducing the ZnO buffer layer, which was a valuable achievement for the growth of MgO-based MTJ.

As shown in Fig. 6.10, the XRD patterns of SiO_2//ZnO 50nm/ NiO 50nm, indicated a good out-of-plane (002) texture of NiO films on (0002) ZnO underlayers, respectively. NiO is an antiferromagnetic material with a rock salt structure. In addition, the lattice constants of the NiO (a=0.418 nm), Fe_3O_4 (a=0.838 nm) and MgO (a=0.420 nm) were quiet slimier. Therefore, NiO could be also served as a structural buffer layer.

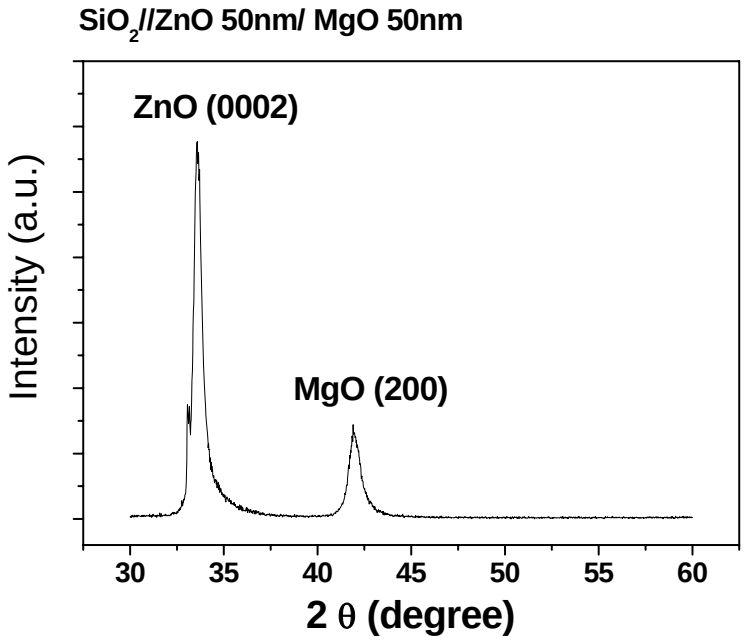

Fig. 6.9. The XRD pattern of SiO_2//ZnO 50nm/ MgO 50nm

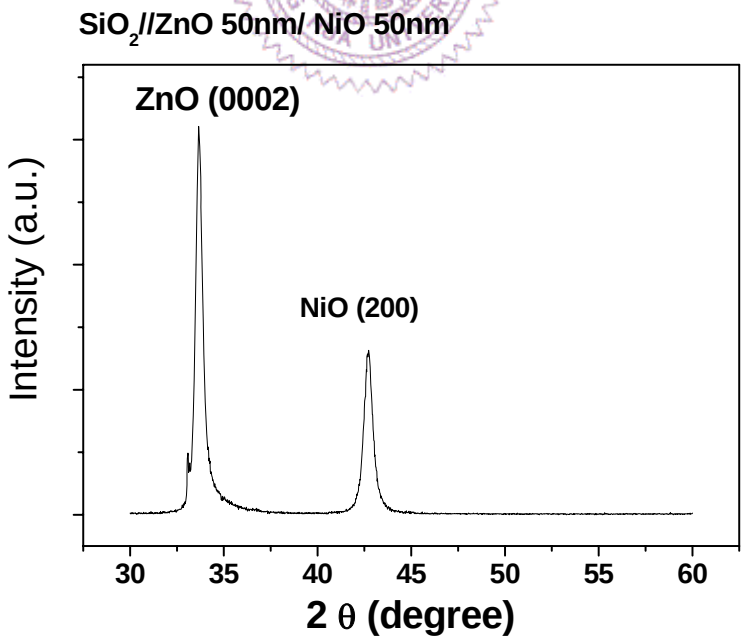

Fig. 6.10. The XRD pattern of SiO_2//ZnO 50nm/ NiO 50nm

However, this layer structure was lacking of a conducting layer as the bottom electrode. Although the ZnO is a semiconductor, the resistance is too high to be used as the electrode. Therefore, in the next step, the conducting material Ag, Cr and TiN were deposited on the ZnO buffer layer.

Since conducting material TiN has a rock salt structure with the lattice constant of 0.41 nm. TiN is one of the good candidates for structural buffer layers and electrodes. However, the XRD patterns of SiO_2//ZnO 50nm/ TiN 30nm as shown in Fig. 6.11, the peak intensity of TiN was not quiet clear, indicated the poor texture of TiN. Another conducting material prepared on ZnO layer is metallic Ag layer. Ag has the best conductivity among the metals. The XRD patterns of SiO_2//ZnO 50nm/ Ag 50nm as shown in Fig. 6.12, indicated a good out-of-plane (111) texture of Ag films on (0002) ZnO underlayers, respectively.

Finally, the metallic Cr layer with cubic structure was deposited on the ZnO buffer layer. As shown in Fig. 6.13, the XRD patterns of SiO_2//ZnO 50nm/ Cr 50nm, indicated a good out-of-plane (110) texture of Cr films on (0002) ZnO underlayers, respectively. In a conventional bottom pinned spin valve structure, the AFM layer would be deposited on the bottom electrode. Therefore, the AFM NiO layer was deposited on the top of the Cr (110) layer. The XRD patterns of SiO_2//ZnO 50nm/ Cr 50nm/ NiO 50nm was shown in the Fig. 6.14. A clear NiO (111) peak indicated the well texture of NiO layer. Beside, the higher exchange coupling strength could be expected from the NiO (111) plane. It is

because the NiO (111) plane was the spin-uncompensated plane. In a brief conclusion, we already obtained the layer structure including the structural buffer layers, a conducting layer and AFM layer with highly texture along the out-of-plane direction.

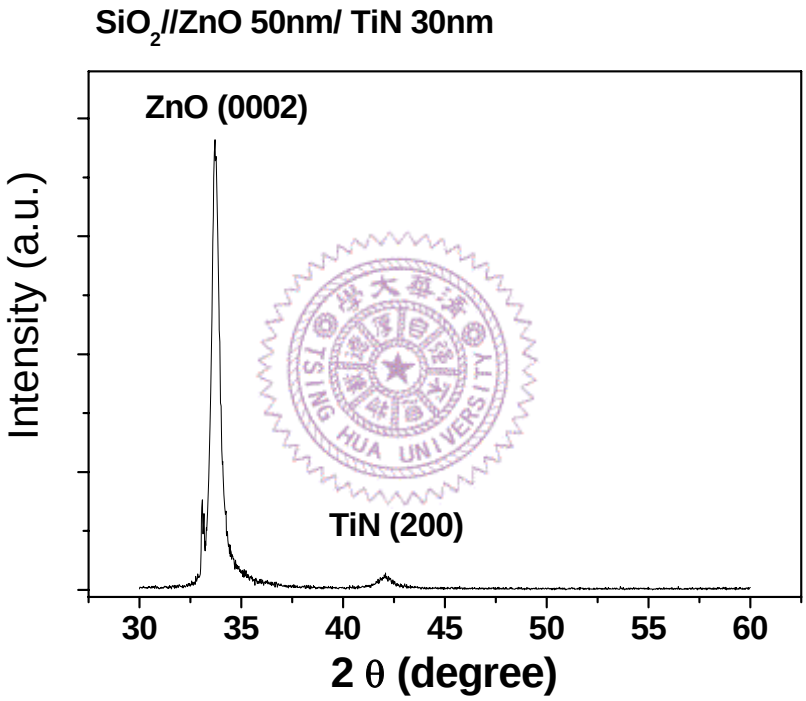

Fig. 6.11. The XRD patterns of SiO_2//ZnO 50nm/ TiN 30nm

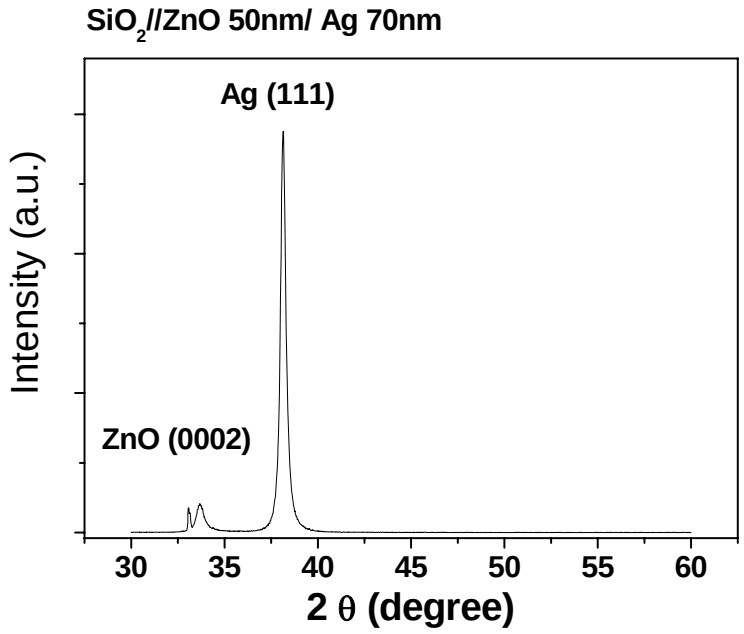

Fig. 6.12. The XRD pattern of SiO_2//ZnO 50nm/ Ag 50nm/ NiO 50nm

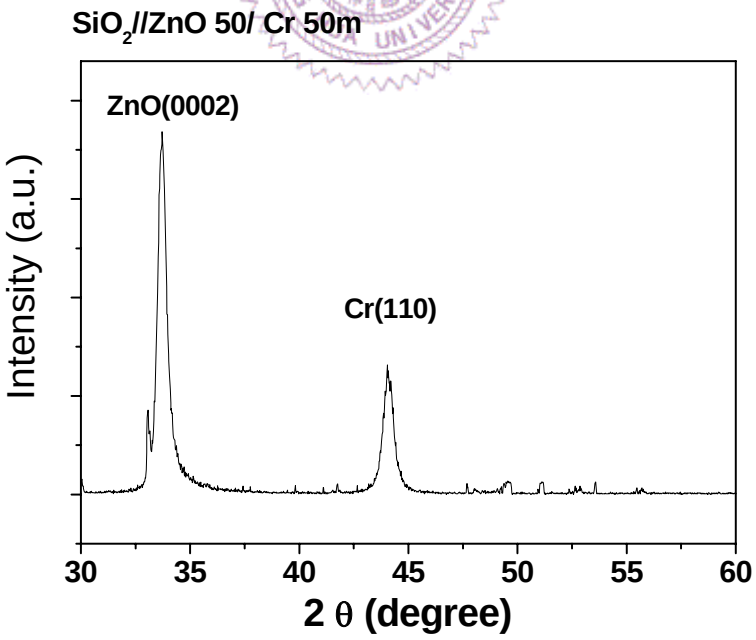

Fig. 6.13. The XRD pattern of SiO_2//ZnO 50nm/ Cr 50nm

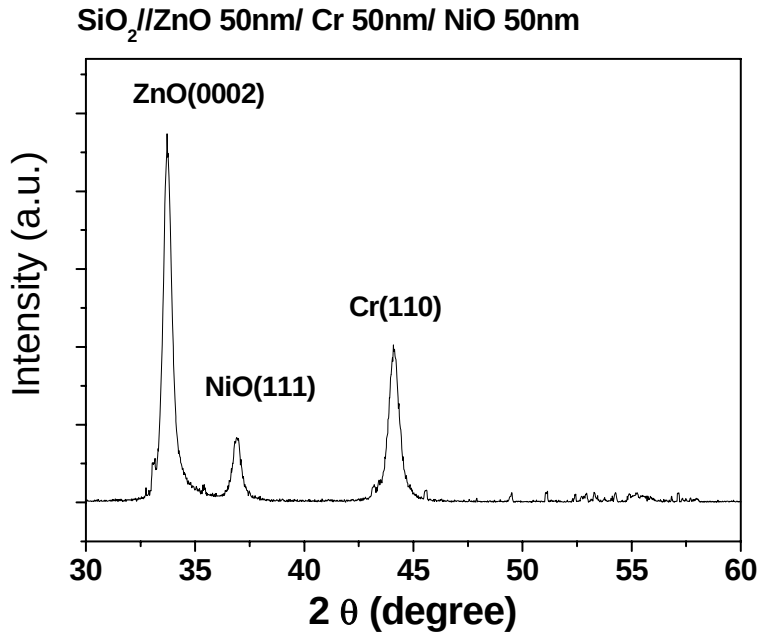

Fig. 6.14. The XRD pattern of SiO_2//ZnO 50nm/ Cr 50nm/ NiO 50nm

The XRD pattern of SiO_2//ZnO 50nm/ Cr 50nm/ NiO 50nm/ Fe_3O_4 50nm was shown in the Fig. 6.15. Fe_3O_4 prepared on the AFM NiO (111) layer, revealed a good (111) orientation along the out-of-plane direction. This layer structure was composed of a conducting electrode, AFM layer and FM layer. It already satisfied the basic requirement for the functional MTJ device. In addition, all layers revealed the highly texture along the out-of-plane direction, which was suitable for MgO barrier growth.

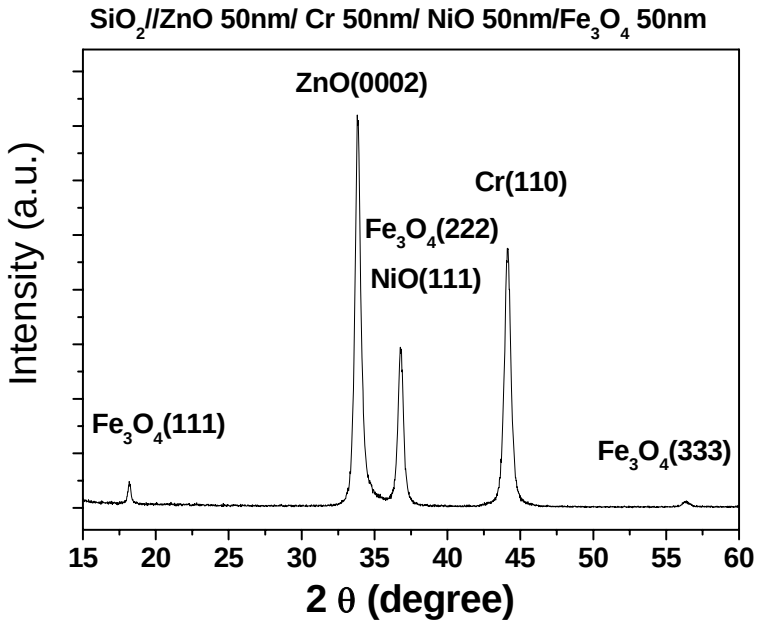

Fig. 6.15. The XRD pattern of SiO_2//ZnO 50nm/ Cr 50nm/ NiO 50nm/ Fe_3O_4 50nm

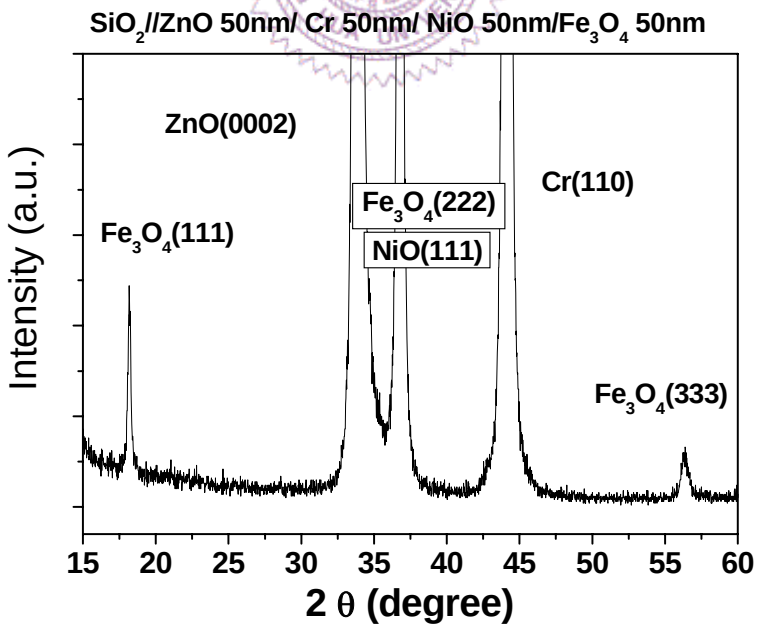

Fig. 6.16. The XRD pattern of SiO_2//ZnO 50nm/ Cr 50nm/ NiO 50nm/ Fe_3O_4 50nm

In the pervious section, the layer structure was suitable for the growth of MgO (111) barrier, which could be obtained by IBD system at room temperature. For comparison, the layer structure was suitable for the growth of MgO (002) barrier, which was also being investigated. In pervious studies, only the MgO (002) type MTJ had the related theory and experiment data to support the extreme high MR ratio. In the pervious section, we mentioned the MgO (002) layer could be grown on the ZnO (0002) underlayer. Therefore, the further improvement of the buffer layer was based on the underlayer of ZnO/MgO layers.

In this experiment, the Fe layer was deposited on the top of the underlayer. According to pervious studies, the BCC structure Fe was one of the most suitable FM layers for MgO-based MTJ. The XRD pattern of SiO_2//ZnO 50nm/ MgO 50nm/ Fe 30nm/ Ta 5nm was shown in the Fig. 6.17. Orientations of Fe (110) and Fe (200) both existed on the top of the MgO layer, which revealed the ZnO/MgO underlayer was not very good structural buffer layers for the growth of Fe (002) layer. In the next step, the thickness dependence of underlayer is discussed. It helps us to understand the structural relationship between the underlayer and FM layer. The XRD pattern of SiO_2//ZnO X nm/ MgO 50nm/ Fe 30nm/ Ta 5nm (X=25, 50, 75 nm) was shown in the Fig. 6.18. The peak intensity of MgO (200) was increased with the thickness of the ZnO underlayer decreased. In addition, the relative peak intensity ratio between the Fe (200) and Fe (110) was also increased with the thinner ZnO underlayer. The XRD pattern of SiO_2//ZnO 50 nm/ MgO X nm/ Fe 30nm/ Ta 5nm (X=25, 50 nm) was shown in the Fig. 6.19. The relative peak intensity

ratio between the Fe (200) and Fe (110) was greatly increased with the thinner MgO underlayer.

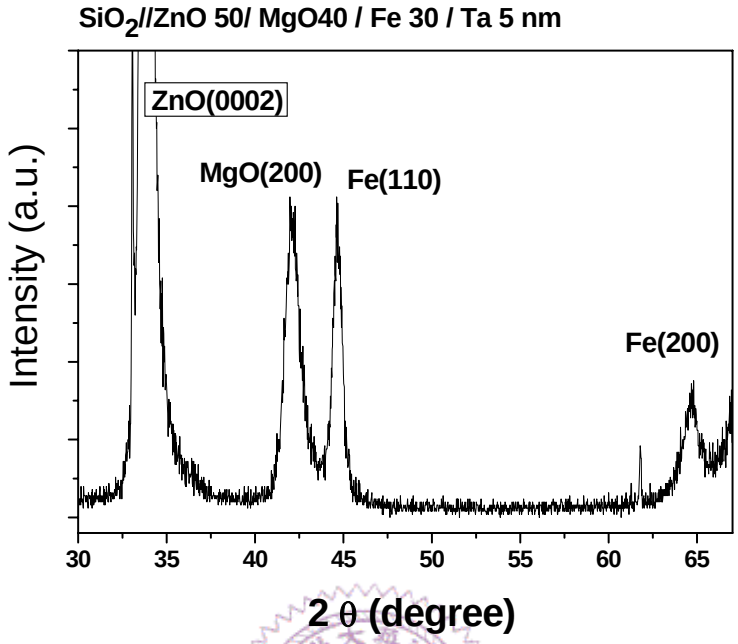

Fig. 6.17. The XRD patterns of SiO_2//ZnO 50nm/ MgO 50nm/ Fe 30nm/ Ta 5nm

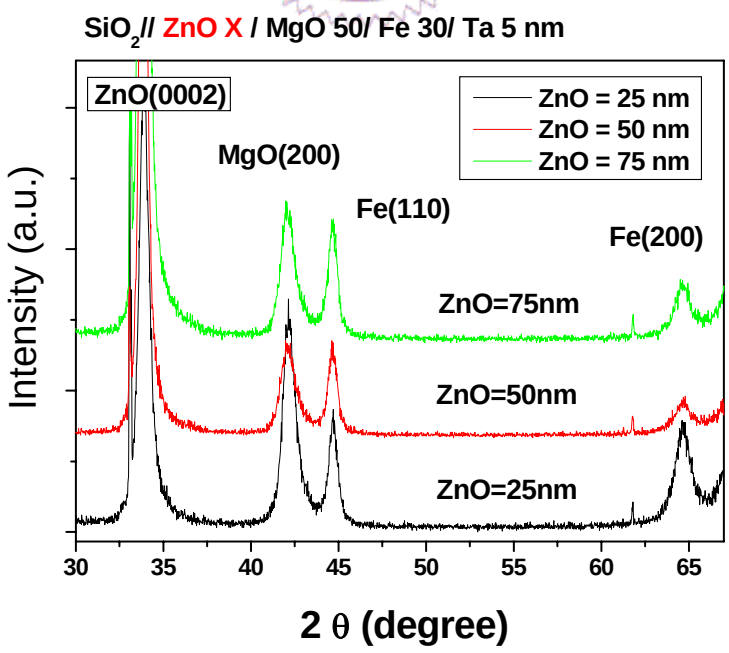

Fig. 6.18. The XRD pattern of SiO_2//ZnO X nm/ MgO 50nm/ Fe 30nm/ Ta 5nm (X=25, 50, 75 nm)

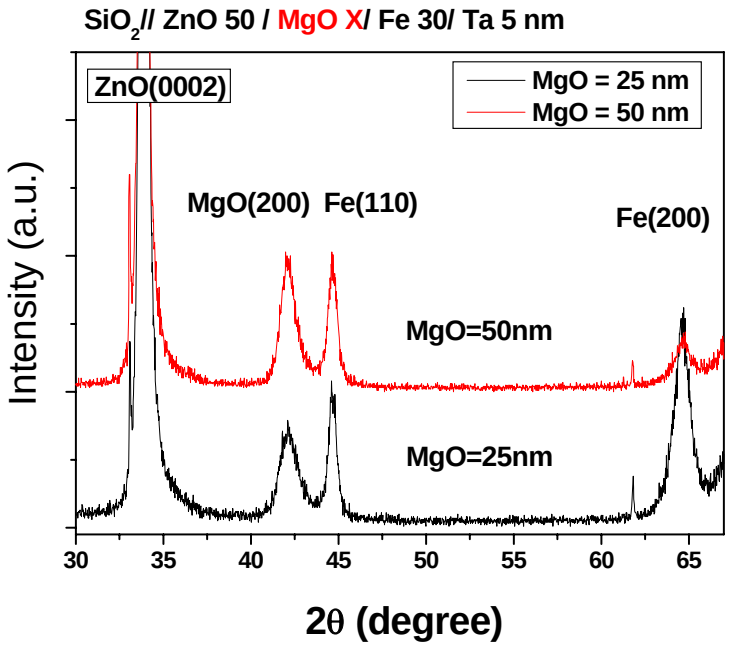

Fig. 6.19. The XRD pattern of SiO_2//ZnO 50 nm/ MgO X nm/ Fe 30nm/ Ta 5nm (X=25, 50 nm)

According to the pervious experiment data, the thinner underlayer was more suitable for the growth of Fe (200) layer. The XRD patterns of SiO_2//ZnO X nm/ MgO Y nm/ Fe 30nm/ Ta 5nm (X=15 Y=10, X=5 Y=5, X=2.5 Y=2.5) were shown in the Fig. 6.20. The peak intensities of the Fe (200) in these samples were almost the same. Therefore, we should focus on the peak intensity of Fe (110). Due to the BCC structure of a pure iron, the natural preferred orientation along the out-of-plane direction should be (110). The reduction of the peak intensity of the Fe (110) was quiet obvious when the ZnO is 2.5 nm and MgO is 2.5 nm. This phenomenon may indicate the thinner MgO layer is more suitable for the growth of Fe (200), which was not consistent with our expected results.

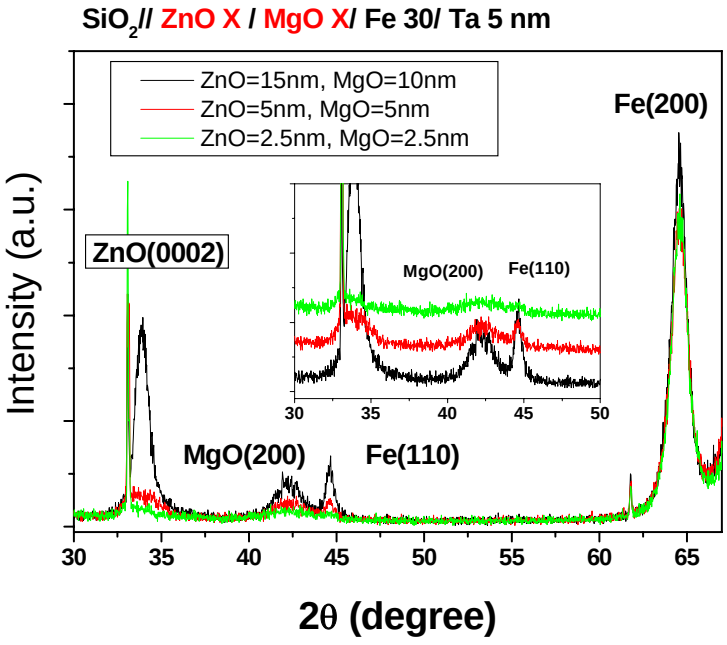

Fig. 6.20. The XRD patterns of SiO_2//ZnO X nm/ MgO Y nm/ Fe 30nm/ Ta 5nm (X=15 Y=10, X=5 Y=5, X=2.5 Y=2.5)

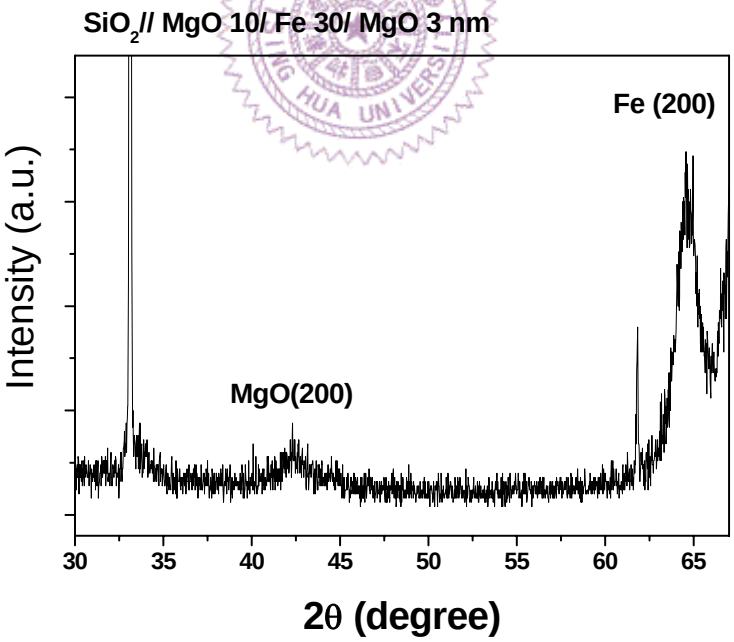

Fig. 6.21. The XRD patterns of SiO_2// MgO 2.5 nm/ Fe 30nm/ Ta 5nm

On the other hand, we may wonder the effect of the ZnO underlayer, because the thickness of ZnO underlayer was only 2.5nm. The XRD patterns of SiO_2// MgO 2.5 nm/ Fe 30nm/ Ta 5nm was shown in the Fig. 6.21. In order to investigate the importance of the ZnO underlayer, we directly deposited the MgO underlayer on SiO_2 substrate. Peak intensity of Fe (200) of sample without the ZnO underlayer was greatly decreasing. It indicated the ZnO layer indeed promote the (200) texture of MgO underlayer. Thinner ZnO layer would have better capability for the growth of MgO (200) layer, which might point out the surface effect play an important role in the growth mechanism. One of the possible reasons is the surface energy or interfacial energy, it may affect the growth preferred orientation of MgO layer. The growth mechanism of this film structure was still not clear. We would have more efforts on it in the future work.

The full stacks of the MgO-based MTJs were fabricated on the underlayer of ZnO/MgO bilayer structure. The XRD patterns of SiO_2// ZnO 2.5nm/ MgO 2.5 nm/ Fe 10nm/ MgO 1nm / Fe 15nm / IrMn 20nm/ Ta 5nm was shown in the Fig. 6.22. Although the clear Fe (200) peak was shown in the Fig. 6.22, the texture of top Fe layer is difficult to identify. It was due to the peaks position of top Fe layer and bottom Fe layer were in the same degree. Besides, IrMn (200) peak was also shown in the Fig. 6.22. Well (200) texture of IrMn layer indicated the (200) texture of the top Fe layer. The hysteresis loop of SiO_2// ZnO 2.5nm/ MgO 2.5 nm/ Fe 10nm/ MgO 1nm / Fe 15nm / IrMn 20nm/ Ta 5nm was shown in the Fig. 6.23. A standard spin-valve film structure enables us to create the controllable parallel and antiparallel states between the pinned layer and

free layer. In a brief conclusion, a typical MgO-based MTJ was fabricated by introducing ZnO/MgO underlayer at room temperature. The device fabrication will be done in the future.

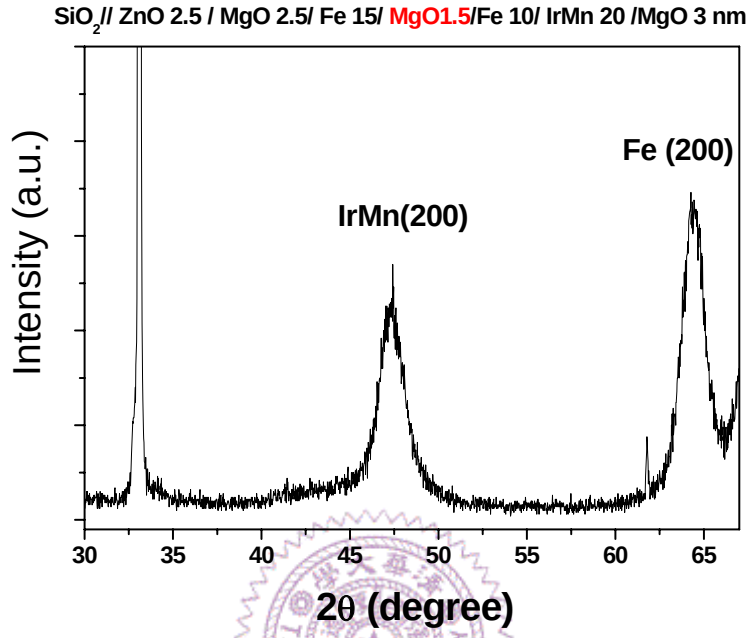

Fig. 6.22. The XRD patterns of SiO_2// ZnO 2.5nm/ MgO 2.5 nm/ Fe 10nm/ MgO 1nm / Fe 15nm / IrMn 20nm/ Ta 5nm

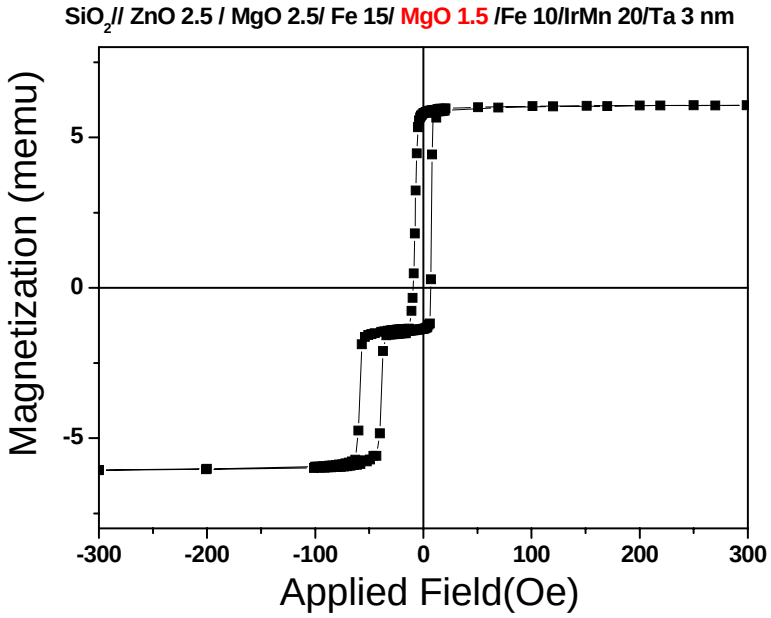

Fig. 6.23. The hysteresis loop of SiO_2// ZnO 2.5nm/ MgO 2.5 nm/ Fe 10nm/ MgO 1nm / Fe 15nm / IrMn 20nm/ Ta 5nm

Furthermore, the Fe_3O_4-baes MTJ was also fabricated by introducing the ZnO/MgO underlayer. The XRD patterns of SiO_2// ZnO 2.5nm/ MgO 2.5 nm/ Fe_3O_4 50nm/ MgO 0.8nm / Fe 10nm / Ta 5nm was shown in the Fig. 6.24. The XRD peaks of (400) Fe_3O_4 and (200) Fe indicated a good out-of-plane (400) and (200) texture of Fe_3O_4 and Fe, respectively. However, the quality of MgO barrier could not be identified from XRD patterns. In order to further investigate the quality of the MgO barrier, cross-sectional TEM analysis was performed. TEM image showed an excellent morphology of the MTJ structure with smooth and flat layers as shown in the Fig. 6.25. High-resolution image showed atomically resolved lattice plane with (100) planes perpendicular to the growth direction. The high-resolution image showed a highly texture of the MgO, upper Fe and lower Fe_3O_4 layers as shown in Fig. 6.26. The top Fe layer is b.c.c. with a (002) structure and the MgO is cubic (rock salt structure) and also (100) textured.

The hysteresis loop of SiO_2// ZnO 2.5nm/ MgO 2.5 nm/ Fe_3O_4 50nm/ MgO 1nm / Fe 5nm / Ta 5nm was shown in the Fig. 6.27. MR ratio is corresponding to the magnetization alignments between the free layer and pinned layer. Therefore, how to independently rotate the free layer is a key issue to obtain the high MR ratio of MTJ. In order to investigate the magnetization rotation behavior of free layer Fe, the minor loop of the full stack was shown in the Fig. 6.28. In the Fig. 6.28, a magnetic field of 1.5 T was applied in the negative direction before the measurement, so we could make sure the magnetization of pinned layer Fe_3O_4 was along the negative direction. In addition, we can reconfirm the configuration

of the magnetization of free and pinned layer through comparing the minor loop and full loop of this sample. The higher magnetization along the negative field direction of the full loop indicated the magnetization of pinned layer still was aligned in the negative direction. Besides, the coincidence between the minor loop and full loop around measuring field (200 Oe), which revealed the rotation of the free layer would not affect the stability of pinned layer magnetization.

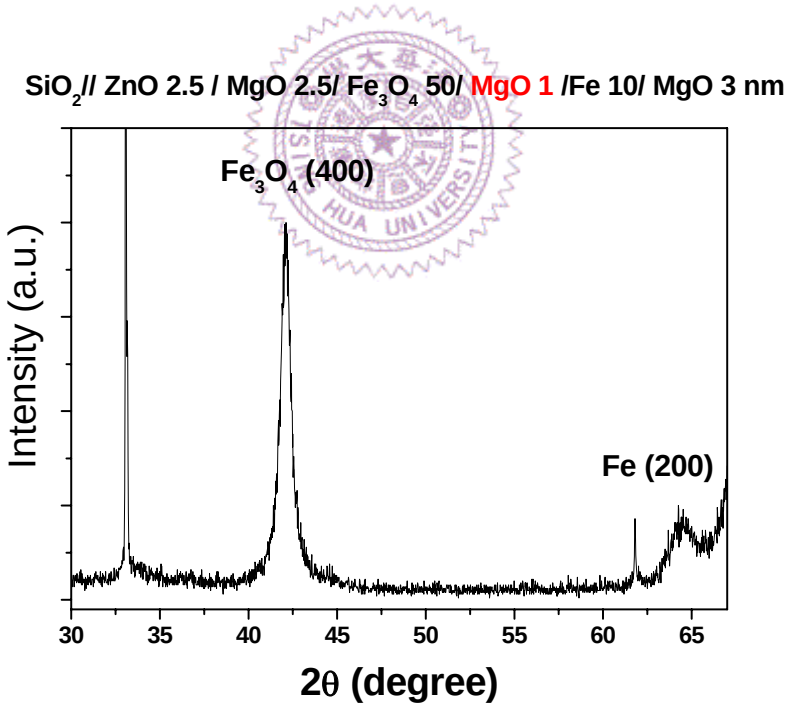

Fig. 6.24. The XRD patterns of SiO_2// ZnO 2.5nm/ MgO 2.5 nm/ Fe_3O_4 50nm/ MgO 0.8nm / Fe 10nm / Ta 5nm

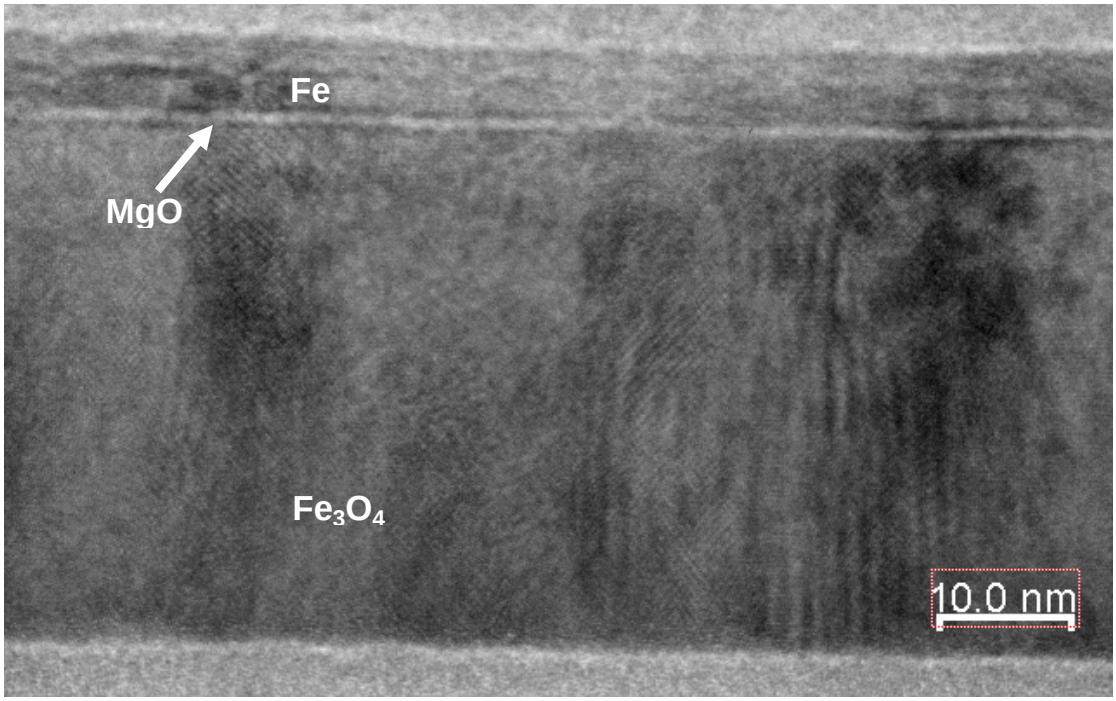

Fig. 6.25. The TEM image of SiO_2// ZnO 2.5nm/ MgO 2.5 nm/ Fe_3O_4 50nm/ MgO 0.8nm / Fe 10nm / Ta 5nm

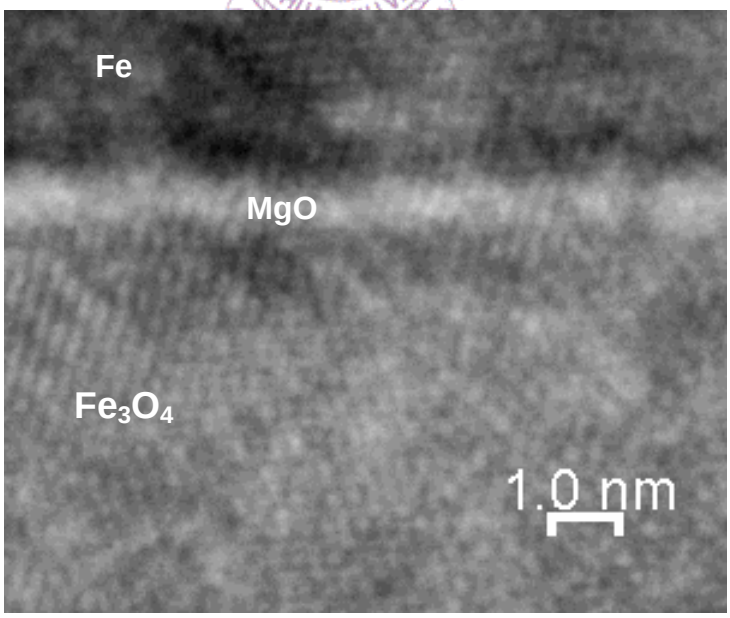

Fig. 6.26. The HR-TEM image of SiO_2// ZnO 2.5nm/ MgO 2.5 nm/ Fe_3O_4 50nm/ MgO 0.8nm / Fe 10nm / Ta 5nm

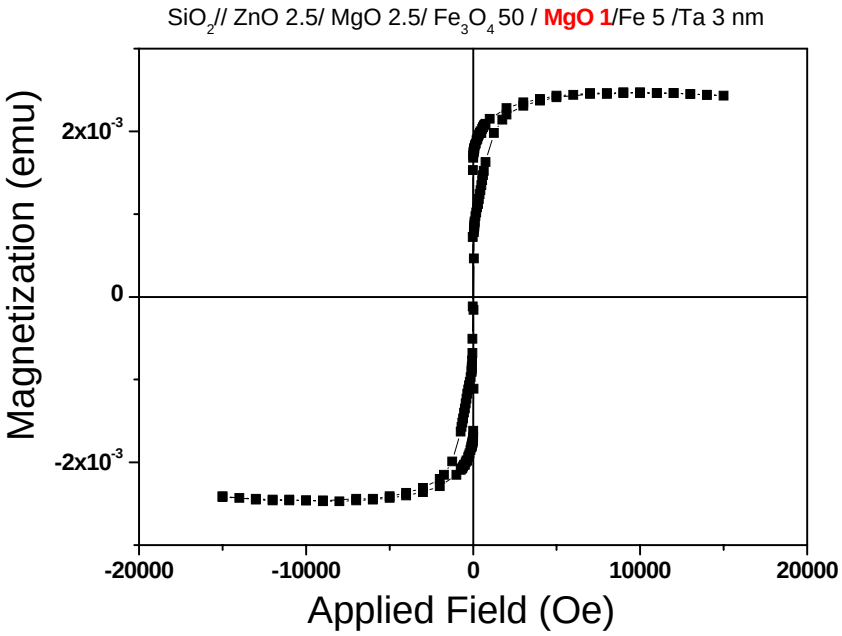

Fig. 6.27. The hysteresis loop of SiO_2// ZnO 2.5nm/ MgO 2.5 nm/ Fe_3O_4 50nm/ MgO 1nm / Fe 5nm / Ta 5nm

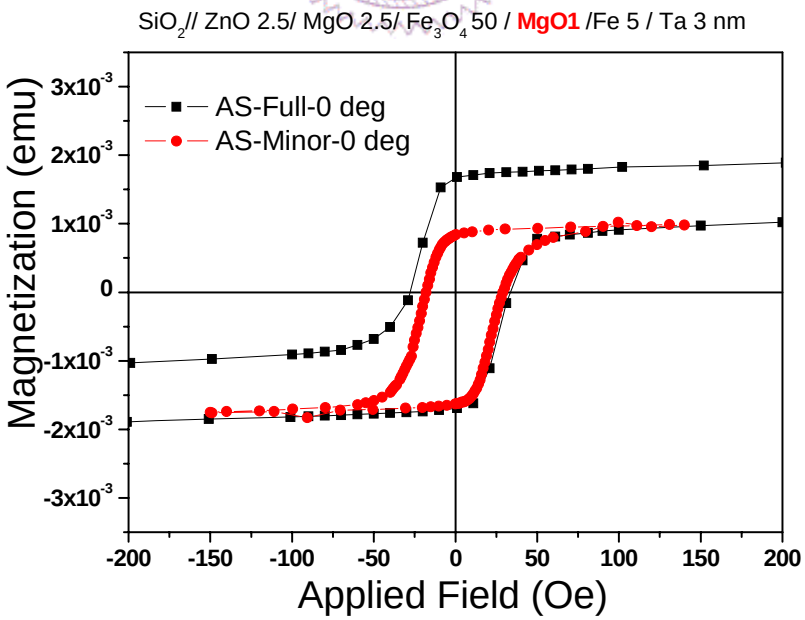

Fig. 6.28. The minor loop of SiO_2// ZnO 2.5nm/ MgO 2.5 nm/ Fe_3O_4 50nm/ MgO 1nm / Fe 5nm / Ta 5nm

Finally, the full oxide based MTJ which combined the Fe_3O_4 and ZnCoO as the FM layers was also fabricated by introducing the ZnO/MgO underlayer. The XRD patterns of SiO_2// ZnO 2.5nm/ MgO 2.5 nm/ Fe_3O_4 50nm/ MgO 2.5 nm / ZnCoO 50nm / Ta 5nm was shown in the Fig. 6.29. The XRD peaks of (400) Fe_3O_4 and (0002) ZnCoO indicated a good out-of-plane (400) and (0002) texture of Fe_3O_4 and ZnCoO, respectively. As mentioned in the last paragraph, in order to further investigate the microstructure of the MTJ, cross-section TEM analysis was performed. TEM image showed an excellent morphology of the MTJ structure with smooth and flat layers as shown in the Fig. 6.30. High-resolution image showed atomically resolved lattice plane with (100) planes perpendicular to the growth direction. High-resolution image showed a highly texture of the MgO, upper ZnCoO and lower Fe_3O_4 layers as shown in Fig. 6.31. We will try to discuss the structural relationship between the MgO and ZnCoO layers in the future work. On the other hand, due to the magnetic moment of Fe_3O_4 is much larger than that of ZnCoO, the switching field of ZnCoO could not be identified in the hysteresis loop of the full stack MTJ.

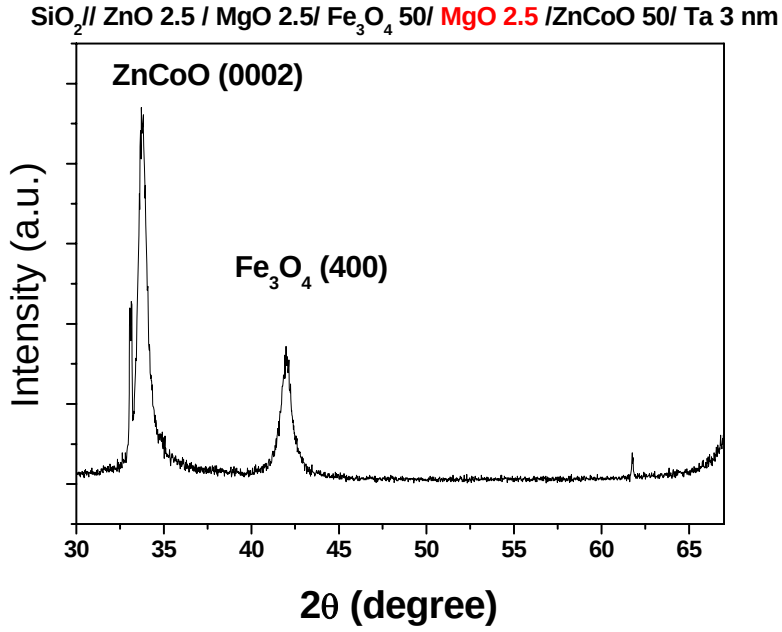

Fig. 6.29. The XRD patterns of SiO_2// ZnO 2.5nm/ MgO 2.5 nm/ Fe_3O_4 50nm/ MgO 2.5 nm / ZnCoO 50nm / Ta 5nm

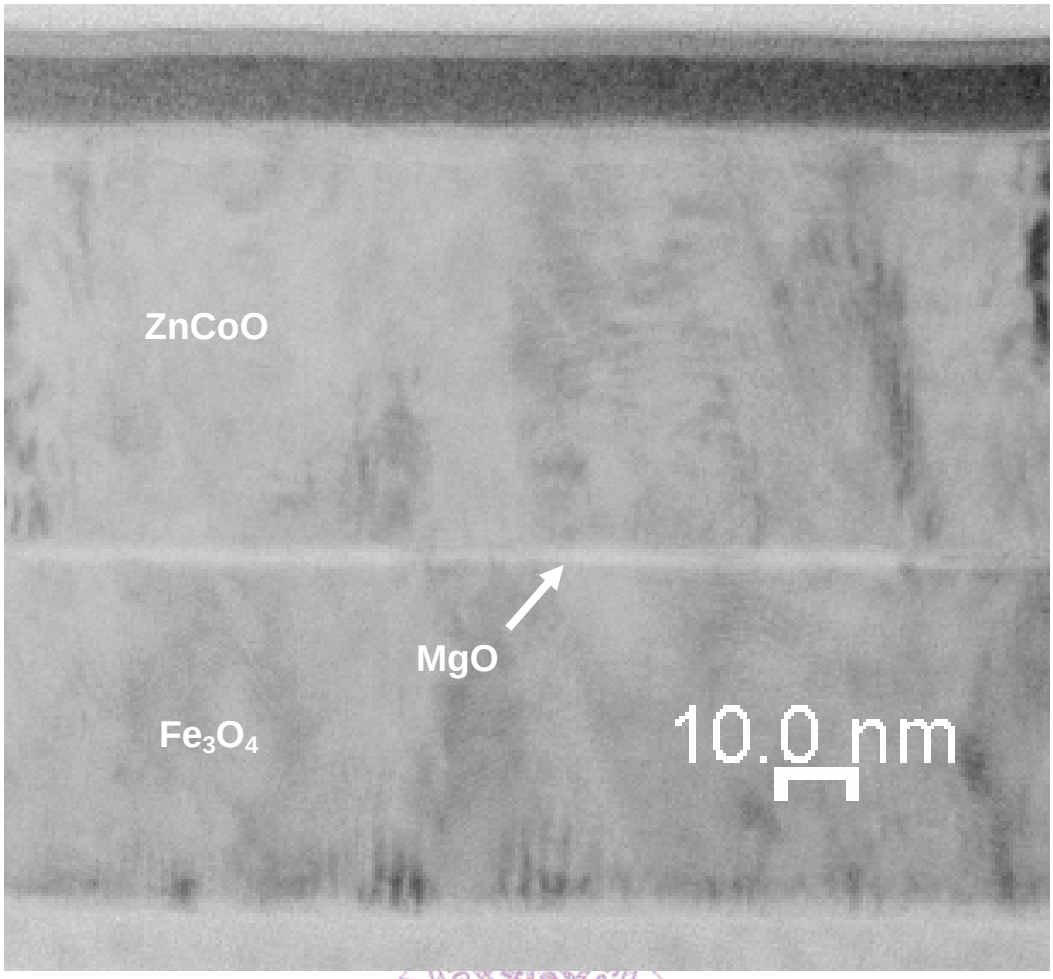

Fig. 6.30. The TEM iamge of SiO_2// ZnO 2.5nm/ MgO 2.5 nm/ Fe_3O_4 50nm/ MgO 2.5 nm / ZnCoO 50nm / Ta 5nm

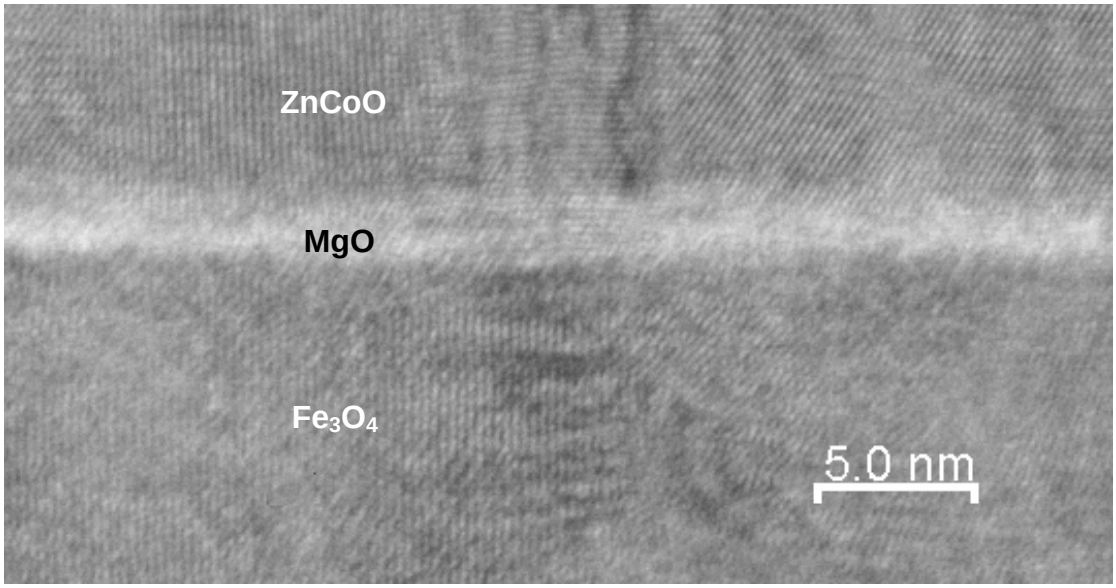

Fig. 6.31. The HR-TEM iamge of SiO_2// ZnO 2.5nm/ MgO 2.5 nm/ Fe_3O_4 50nm/ MgO 2.5 nm / ZnCoO 50nm / Ta 5nm

In a brief conclusion, we could obtain the MTJ with the texture of MgO (111) and MgO (200) by introducing the different underlayer. However, if the sheet films were fabricated into device, there are still some problems. For example, Fe_3O_4 is difficult to handle in ICP (Induce Coupling Plasma) etching process. In a typical ICP etching process, the etching gas would react with material to form the product which could be easily taken away with etching gas. In this situation, the re-deposition problem on the side wall of the MTJ could be effectively reduced. However, the only one suitable etching gas for Fe_3O_4 material is Ar. The problem is that the Ar would not react with Fe_3O_4 to form any gas-phase product. Therefore, the etching of Fe_3O_4 material would re-deposit on the side wall of MTJ or attach to the chamber and would become pollutions. In order to solve this problem, we decided to use the lift-off process to fabricating the MTJ device. In a conventional lift-off

process, it needs to break the vacuum for the patterning of bottom electrode. It may result in the incorporation of defects and oxidation of the surface. For this reason, the bottom electrode could not be served as the structural buffer layer, simultaneously. Therefore, the sample with MgO (111) layer is not suitable for the lift-off process, due to the Cr bottom electrode. On the other hand, in the sample with MgO (200) texture, the amorphous Ta bottom electrode was inserted between the SiO_2 substrate and ZnO/MgO underlayer. The XRD pattern of SiO_2// Ta 20 nm/ ZnO 2.5nm/ MgO 2.5 nm/ Fe 30nm/ Ta 5nm was shown in the Fig. 6.32. The XRD peaks of (200) Fe indicated a good out-of-plane (200) texture of Fe could be obtained on the Ta bottom electrode.

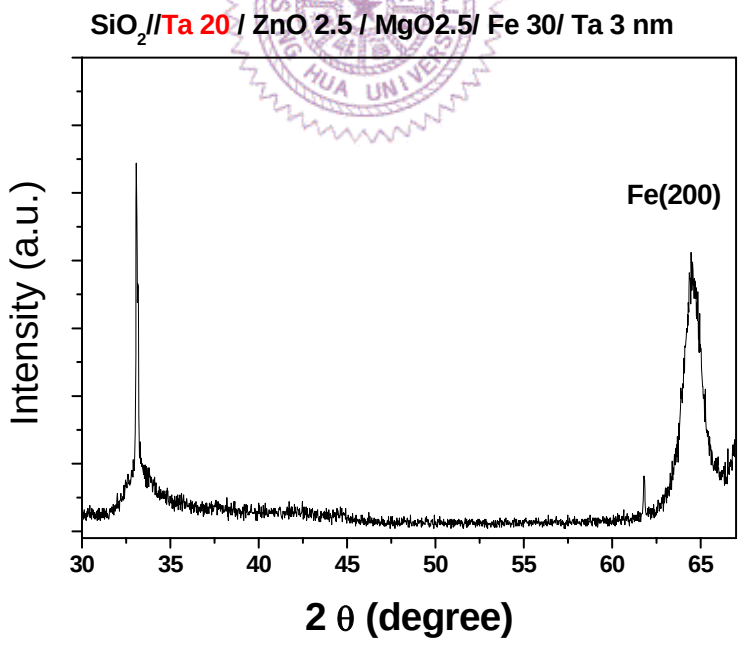

Fig. 6.32. The XRD pattern of SiO_2// Ta 20 nm/ ZnO 2.5nm/ MgO 2.5 nm/ Fe 30nm/ Ta 5nm

6.3.d Full stack

We prepared the full stack MTJs of SiO_2// Ta 20nm/ ZnO 2.5nm/ MgO 1.2nm/ Fe_3O_4 50nm/ MgO 3nm/ ZnCoO 50nm/ Ta 10nm. This layer structure included a conducting electrode which was suitable for lift-off process, a texture MgO barrier with a sharp interface and highly texture FM layer. In addition, the full stack MTJ was fabricated at room temperature.

As mentioned in the last section, the MTJ device was fabricated by using the lift-off process. The junction size was 25*25 μm^2. The electric properties were measured by using the PPMS (Physical properties measurement system).

In this section, the brief introduction of pattern process would be introduced. The major fabrication steps were shown in the Fig. 6.33. First, the etching procedure was performed to pattern the bottom electrode (Ta 20nm). The etching process was stopped at the interface between the Ta and SiO_2. The next step was to pattern the cell (MTJ junction), which defines the active junction area. The cell size was 25×25 μm^2. For the lift-off procedure, photoresist was coated to bottom electrode, exposed and developed to the desired cell pattern. All the layers of MTJs including the ZnO/MgO buffer layer were deposited on this patterned bottom electrode. A solvent was then used to dissolve the photoresist, leaving the layers that were in contact with the bottom electrode. Thus, the cell part was patterned. Since the bottom and top

electrodes were needed to be electrically insulated, the insulator (SiO_2) was deposited around the MTJ cell. After this step, patterning process was used in order to make a contact window for top electrode. The SiO_2 located on top of the MTJ cells, which was etched away in ICP etcher. Finally, another lift-off process was used to fabricate the top electrodes. Before depositing the top electrodes, to clean the exposed surface, a sputtering etching process was executed at 50mTorr with a RF power of 100W for 15 sec. The top electrode of Cu 25nm/ Pt 25nm was deposited on the contact windows. The final structure is shown in the Fig. 6.34.

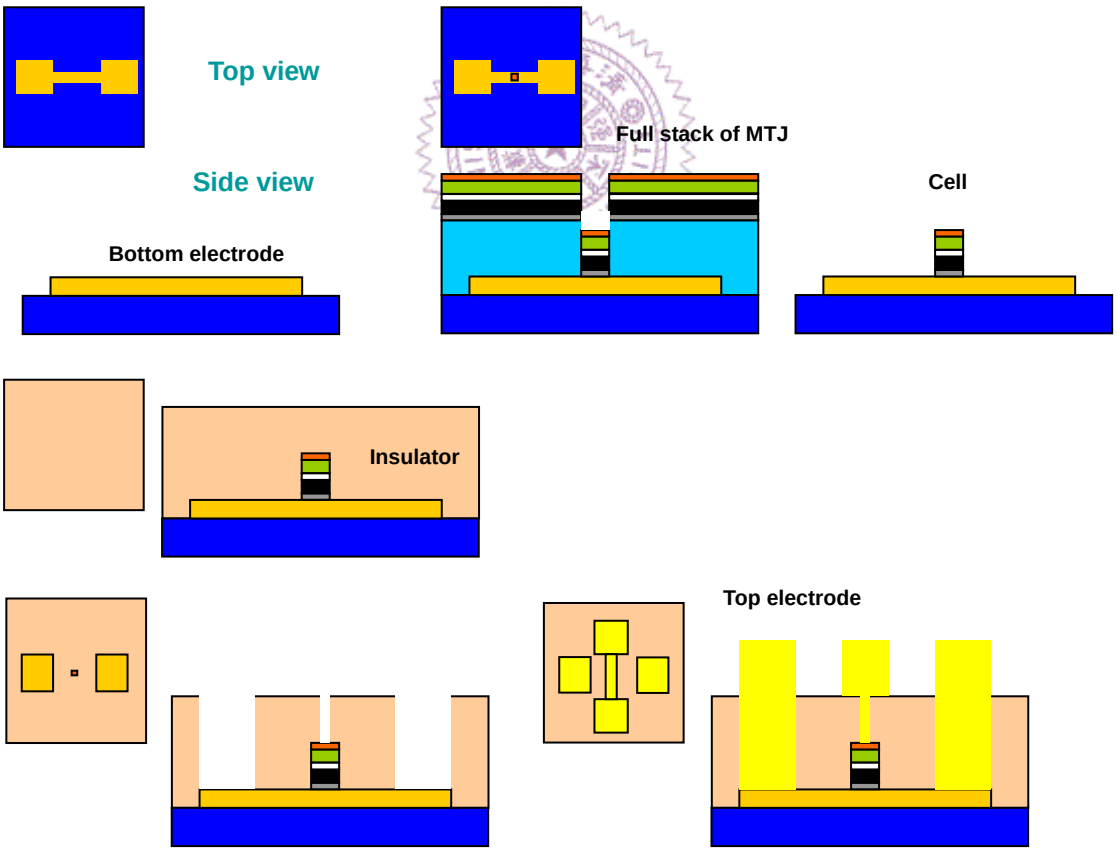

Fig. 6.33. The scheme of the major steps of the lift-off process

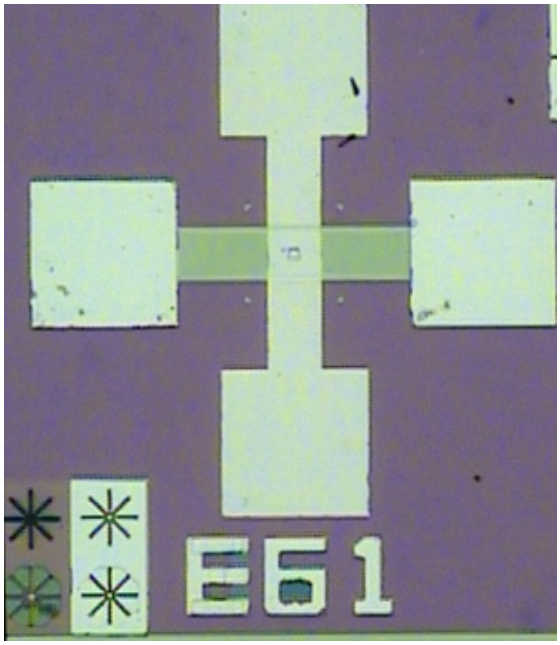

Fig. 6.34. The top view image of the patterned MTJ

Fig. 6.35 shows the I-V curve for the MTJ patterned by lift-off process. The non-linear characteristics indicated electrical transport was dominated by tunneling behavior. By fitting the I-V data into Simmon's equation, effective barrier height and effective barrier thickness of 1.90 eV and 2.189 nm, respectively, could be obtained [5]. Relative low barrier thickness might result from the pin hole or defects in the MgO barrier. We should notice that even the MgO underlayer was only 1.2 nm, it would also contribute to electrical transport behavior and affect the effective barrier thickness fitted from the I-V curve. Furthermore, the relative high resistance from the underlayer ZnO / MgO would reduce the MR ratio for the MTJs. In the future work, we would focus on the reduction of the underlayer and insertion of conducting layer. In addition, the R-H loop of the full oxides stack MTJ was measured at 300K was shown in the Fig.

6.36. The applied magnetic filed was along to the in-plane direction. The MR (MagnetoResistance) of this data was 1.73%. The MR behavior demonstrated the patterned full stack oxide based MTJ was working well. However, it is difficult to identify the plateau of the R-H curve due to the large background signal noise. The R-H loop of the full oxides stack MTJ was measured at 150K, which was shown in the Fig. 6.37. The MR of the R-H loop was increased to 2.68%. It might result from the reduction of the thermal frustration of the magnetic moment. Furthermore, the clear plateau of the R-H curve could be clearly observed in the low field region, which was shown in the Fig. 6.38. A clear plateau in the R-H curve represented the typical pseudo-spin valve switching behavior.

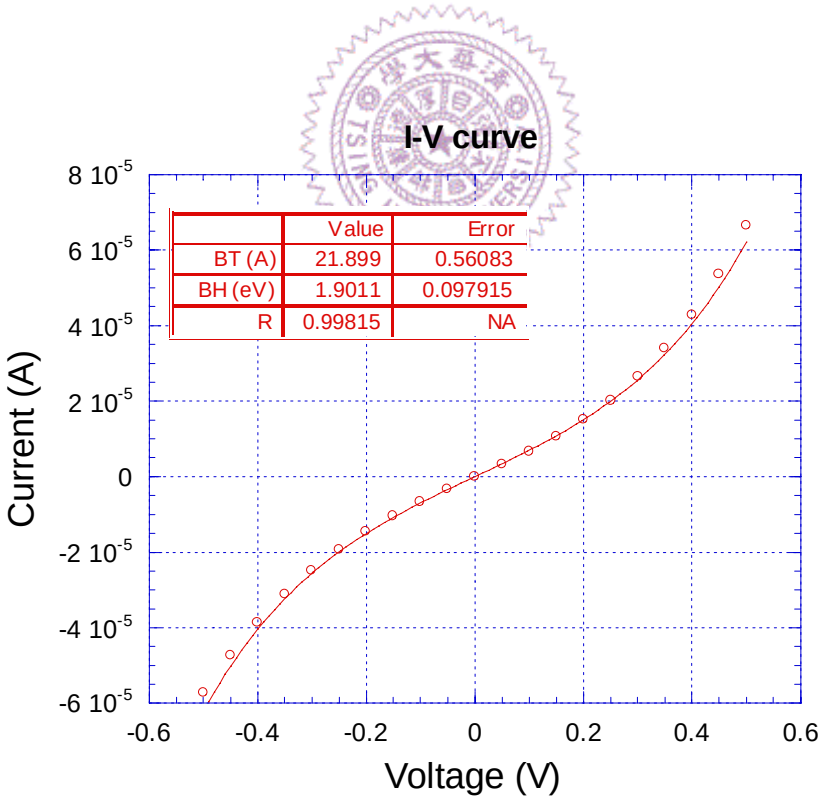

Fig. 6.35. The I-V curves for the MTJ patterned by lift-off

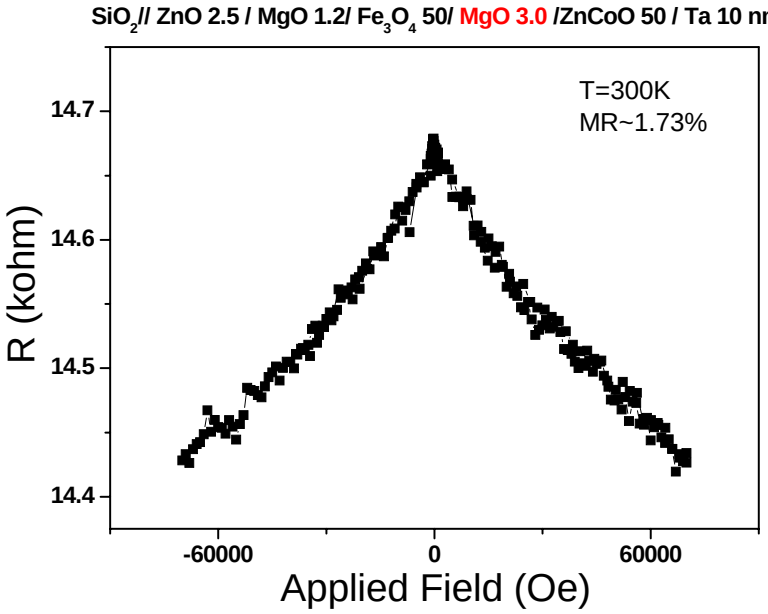

Fig. 6.36. The R-H loop of SiO_2// Ta 20nm/ ZnO 2.5nm/ MgO 1.2nm/ Fe_3O_4 50nm/ MgO 3nm/ ZnCoO 50nm/ Ta 10nm was measured at 300K

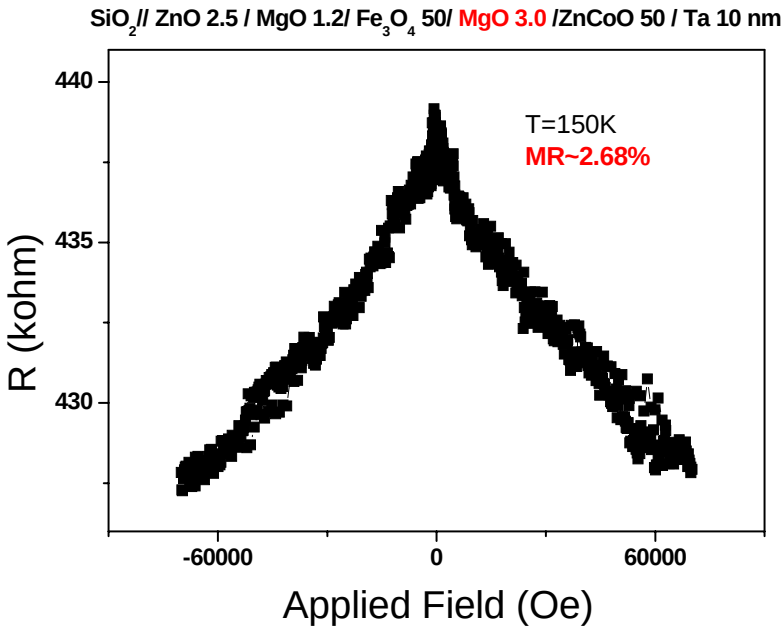

Fig. 6.37. The R-H loop of SiO_2// Ta 20nm/ ZnO 2.5nm/ MgO 1.2nm/ Fe_3O_4 50nm/ MgO 3nm/ ZnCoO 50nm/ Ta 10nm was measured at 150K

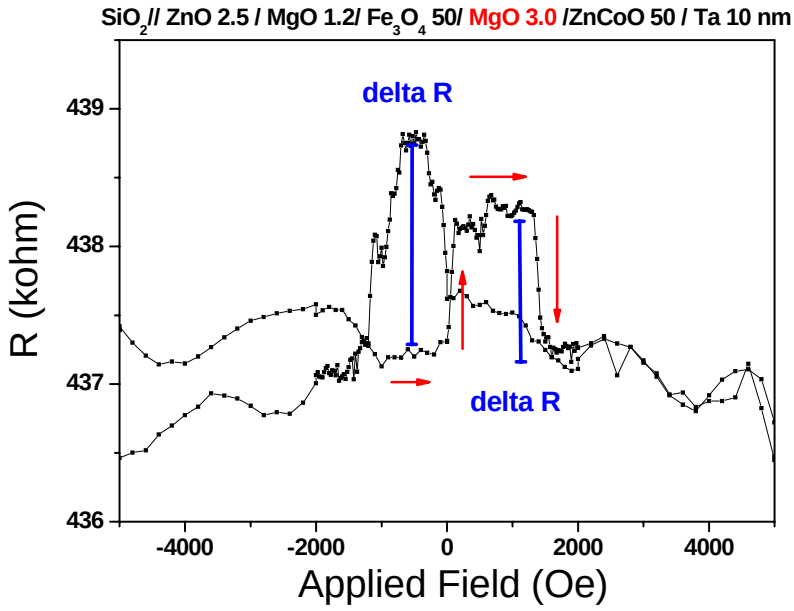

Fig. 6.38. The R-H loop of SiO_2// Ta 20nm/ ZnO 2.5nm/ MgO 1.2nm/ Fe_3O_4 50nm/ MgO 3nm/ ZnCoO 50nm/ Ta 10nm was measured at 150K

In order to further investigate the MR behavior, the magnetic field was applied along the out-of-plane direction. The R-H loop of the full oxide stack MTJ with an applied field along the out-of-plane direction was measured at 150K, which was shown in the Fig. 6.39. The plateau of the R-H curve was hard to identify in the low-field region, which was shown in the Fig. 6.40. The plateau feature only appeared in the R-H curve with applied field along the in-plane direction. This was because the anisotropy of Fe_3O_4 was along the in-plane direction. In other words, the magnetic moment of Fe_3O_4 is easier to keep the stable state in the low-field region when the applied field was along the in-plane direction. It might indicate the tunneling magnetoresistance behavior indeed occurred between the Fe_3O_4 and ZnCoO through MgO barrier. This was a clear evidence to prove that DMS could provide the spin-polarized

electrons.

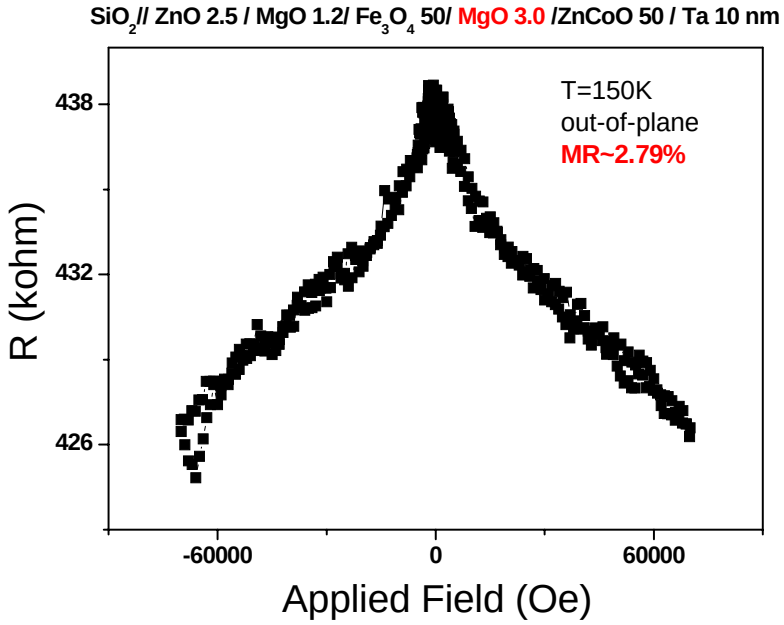

Fig. 6.39. The out-of-plane R-H loop of SiO_2// Ta 20nm/ ZnO 2.5nm/ MgO 1.2nm/ Fe_3O_4 50nm/ MgO 3nm/ ZnCoO 50nm/ Ta 10nm was measured at 150K

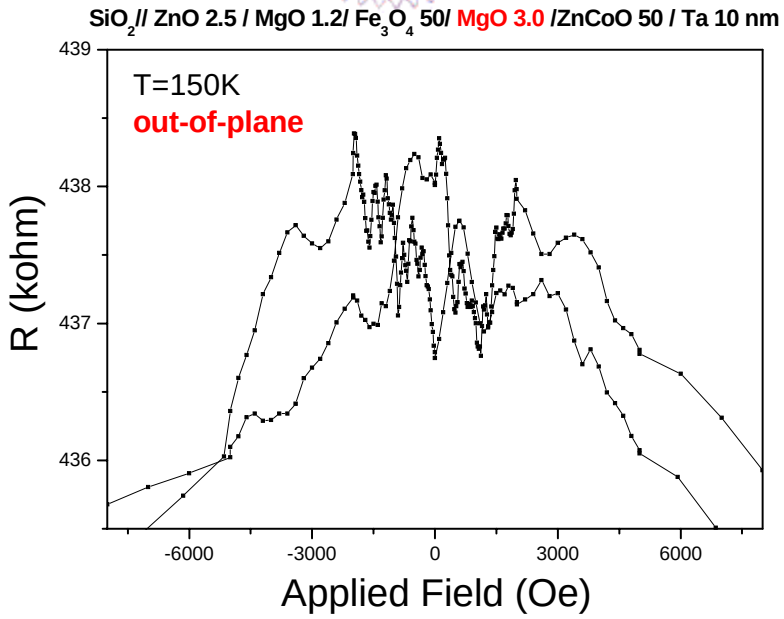

Fig. 6.40. The out-of-plane R-H loop of SiO_2// Ta 20nm/ ZnO 2.5nm/ MgO 1.2nm/ Fe_3O_4 50nm/ MgO 3nm/ ZnCoO 50nm/ Ta 10nm was measured at 150K

On the other hand, the long tail of the MR curve in the high field region was not clear. One possibility is the extreme high saturation field of the Fe_3O_4. The saturation field of the Fe_3O_4 was even higher than 15T. A long tail of the MR curve in the high field region might indicate the magnetic moment of two FM layer were not perfect parallel even under the magnetic field of 7T. Another possibility was attributed to the Fe_3O_4 layer. According to the report, Fe_3O_4 could contribute to the similar MR shape in the high field region [6]. The R-H loop of SiO_2// ZnO 2.5nm/ MgO 2.5nm/ Fe_3O_4 50nm measured at 150K was shown in the Fig. 6.41. The Pt top electrodes with diameter of 1 mm were prepared with hard mask process. The four-point current-in-plane (CIP) measurement was also performed by using PPMS. The magnetic field was also along the in-plane direction. The long tail of the MR curve in the high field was also observed in the Fig. 6.41. However, the MR of this curve was only 0.5%. This result may imply that the MR of the oxide MTJ may be composed of the tunneling magnetoresistance from the MTJ and Fe_3O_4 itself.

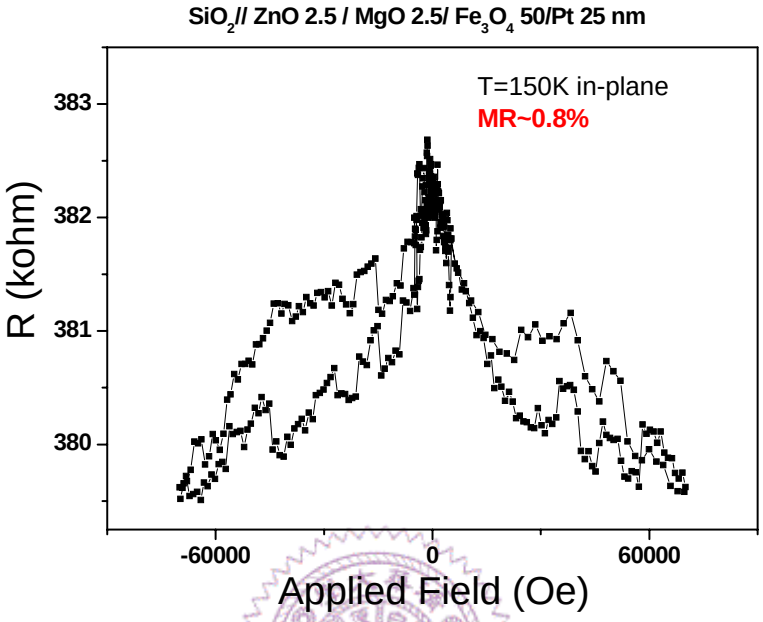

Fig. 6.41. The R-H loop of SiO_2// Ta 20nm/ ZnO 2.5nm/ MgO 2.5nm/ Fe_3O_4 50nm was measured at 150K